Optimization of Sensing Stators in Capacitive MEMS Operating at Resonance

Attilio Frangi, Giacomo Laghi, Giacomo Langfelder, Paolo Minotti, and Sarah Zerbini

I. Introduction

THE REALIZATION of an inertial measurement unit based on multi-axis microelectromechanical systems (MEMS) devices integrated in the same chip is of great interest in several fields of application [1]. In this context several inertial MEMS (gyroscopes [2], [3] and magnetometers [4]) operate with at least one mode excited at resonance, with frequencies in the order of tens of kilohertz. For a given input quantity to be measured this allows to obtain the maximum output signal as described by the behavior of a second-order under-damped system [5].

Most of these sensors exploit a capacitive readout: the input signal (angular rate or magnetic field) is transduced in a capacitance variation, which can be detected by suitable readout electronics.

If F is the force to be detected, the overall sensitivity S of these sensors, i.e. the capacitive signal variation per unit input force ($S = \Delta C/\Delta F$), can be split into two sub-sensitivities: the mechanical sensitivity $\Delta x/\Delta F$, that describes the displacement of the moving mass as a function of the force, and the electrostatic sensitivity $\Delta C/\Delta x$, that relates the displacement with its corresponding capacitance variation.

One typical readout scheme used for these sensors is the parallel plate configuration [5], where the sensing arms on the moving mass are surrounded by two continuous stators; these three elements form a differential capacitor, whose variations can be detected through suitable capacitive sensing interfaces.

Standard parallel plate designs have an intrinsic limitation in that an increase in the sensing area (by using longer stators or several sensing cells in parallel) does not lead to any increase in the value of the sensitivity, when operating at resonance [6]. Indeed, since typical MEMS air gaps are few micrometers wide and typical pressures are in the order of 10^{-3} bar, the free molecule flow regime applies and squeeze film damping dominates [7]. In these operating conditions, though the electrostatic sensitivity linearly increases with the sensing area, the mechanical sensitivity correspondingly decreases by the same amount due to an increase in the damping coefficient, in this linear pressure range.

Effective strategies to increase the sensitivity consist in using higher quality factors, obtained through a reduction of the damping coefficient, which in turn can be accomplished by using lower packaging pressures. However, there is one main reason that discourages this approach: in industrial MEMS processes, it is difficult to obtain pressures lower than fractions of mbar with a good repeatability from part to part [8]. It should be noted that existing technologies allow to build in a single chip devices with separate cavities, each one at a different pressure; in this way, different sensors, each with its own pressure requirement, can be succesfully integrated in a multi-axis inertial measurements unit.

The purpose of this work is to study alternative topologies which improve the mechanical sensitivity $\Delta x/\Delta F$ through a reduction in the damping coefficient, without acting on the pressure of the package in order to avoid the mentioned fabrication and packaging issues. Indeed, with a suitable change in the geometry of the sensing stators, the damping coefficient is lowered, leading to an improvement of the quality factor. This is obtained without worsening the electrostatic sensitivity $\Delta C/\Delta x$, thus guaranteeing a higher overall sensitivity.

The geometry is optimized through a segmentation of the stators (Fig. 1), which considerably decreases the mechanical dissipation while preserving the capacitance variation per unit displacement [9]. The mechanical dissipation (i.e. the damping coefficient) is reduced by allowing an escape route for air molecules present in the gap between the rotor and the stators. Furthermore, for technological reasons, this principle is verified with two suitable structures, formed by a clamped-clamped beam (rotor) and properly designed stators.

Manuscript received September 30, 2014; revised October 24, 2014; accepted December 8, 2014. The work was supported by the European Nanoelectronics Initiative Advisory Council through the Lab4MEMS Project under Grant 325622. Subject Editor A. Luque.

A. Frangi is with the Department of Civil and Environmental Engineering, Politecnico di Milano, Milan 20133, Italy (e-mail: attilio.frangi@polimi.it).

G. Laghi, G. Langfelder, and P. Minotti are with the Department of Electronics, Information, and Bioengineering, Politecnico di Milano, Milan 20133, Italy (e-mail: giacomo.laghi@polimi.it; giacomo.langfelder@polimi.it; paolo.minotti@polimi.it).

S. Zerbini is with the Analog, MEMS, and Sensor Division, STMicroelectronics, Castelletto 20010, Italy (e-mail: sarah.zerbini@st.com).

Color versions of one or more of the figures in this paper are available online.

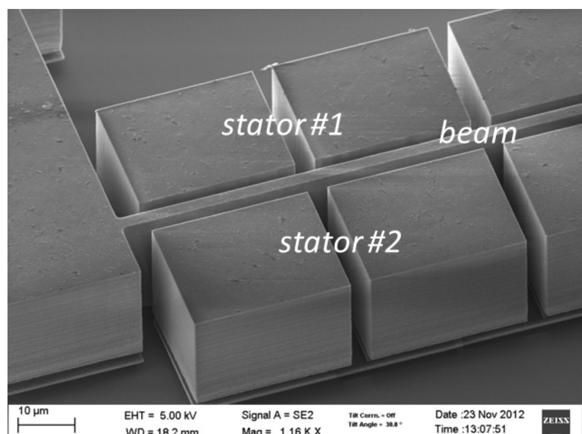

(a)

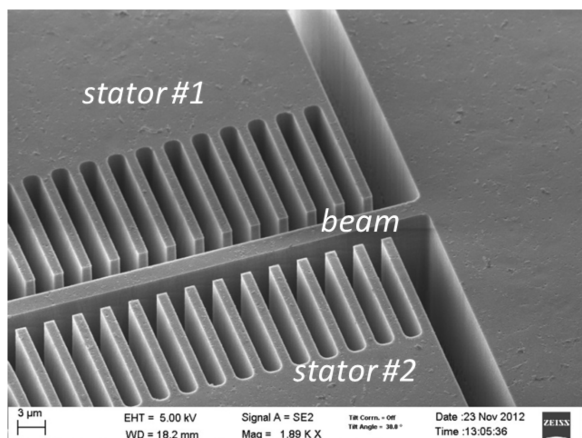

(b)

Fig. 1. Scanning Electron Microscope (SEM) pictures of the two structures tested in this paper, showing the resonant beam surrounded by stators on both sides. In 1a and 1b, the *Block-shaped Stators* (BS) device and the *Comb-shaped Stators* (CS) one are shown, respectively. The fragmentation of the sensing stators, obtained through suitable etching operation, allows a reduction of the mechanical dissipation. (a) BS device. (b) CS device.

The considerable improvements in the overall sensitivity predicted by simulations based on the rarefied gas theory are demonstrated by experimental results: in a representative example, the beams are driven by an AC current at resonance and used as Lorentz-force-based magnetometers [4]. It is experimentally demonstrated that, in this condition, one proposed structure shows an overall sensitivity which is 3× better than what obtained on devices based on continuous parallel plate stators and packaged in the same pressure conditions [6].

II. Theory and Designed Structures

A. Description of the Devices

Two different configurations of the sensing stators are proposed and analyzed in this work. In the first one, a clamped-clamped beam is placed within two stators where suitable interruptions have been etched (BS, *Block-shaped Stators*), as shown in Fig. 1a. In the second one, the beam is designed within two *Comb-shaped Stators* (CS), as visible in Fig. 1b.

Devices were built using the ThELMA (Thick Epitaxial Layer for Microactuators and Accelerometers) process from ST Microelectronics, currently used for mass production of accelerometers and gyroscopes [10].

The beam length and the process thickness are 987.6 μm and 22 μm respectively. The beam width is nominally 3.4 μm, with a $\pm$ 0.15 μm tolerance.

The nominal air gap between the beam and the stators is 2.4 μm and 2 μm for the BS and CS devices respectively. The possibility to use a smaller gap for the CS structure is allowed by the technology. Though there is not a specific DRC rule, when the gap between the beam and the stators is too narrow, the dry hydrofluoric acid (HF) attack is not effective in etching the oxide beneath polysilicon and releasing the suspended beam as desired. This sets the limit on the smallest admissible gap. In the case of the CS structure, the length of the regions where the gap is small is very limited and comparable to the gap size itself (see Fig. 1b). This enables reducing the gap without issues in the release process, as demonstrated by the correct operation of these devices. The gap of 2 μm for the CS design is used to compensate the lower sensitivity caused by its smaller facing area.

Each BS is formed by 30 blocks (29.3 μm long and 23.7 μm deep) separated by a 3.5 μm air gap. The electrical connection of the blocks is guaranteed by a high-conductivity polysilicon route placed beneath the structure. Comb-shaped stators are composed of 306 comb fingers (1.2 μm thick and 14.3 μm deep) laterally separated by a 2 μm air gap.

For the estimation of mechanical parameters, in the framework of the Finite Element Method, equilibrium is enforced in a weak form via the Principle of Virtual Power for slender beams. Let y be a coordinate running along the axis of the beam and x an axis orthogonal to y in the direction of the gap (see Fig. 3). We assume that the beam displacement occurs only in the x direction with component $w(y)$.

The problem is formulated as follows [11]. Find a kinematically compatible displacement field $w(y,t) \in \mathcal{C}$ such that:

$$\int_0^L \rho A \ddot{w}(y,t)\tilde{w}(y)\mathrm{d}y + \int_0^L EJ w''(y,t)\tilde{w}''(y)\mathrm{d}y = \int_S f(\mathbf{x},t)\tilde{w}(y)\mathrm{d}S \qquad \forall \tilde{w} \in \mathcal{C}, \tag{1}$$

where $\tilde{w}$ is a virtual velocity field; $\mathcal{C}$ is a suitable space of sufficiently continuous functions u such that $u(0) = u'(0) = u(L) = u'(L) = 0$; ρA is the mass per unit length; EJ is the bending stiffness; $f(\mathbf{x},t)$ is the x component of the forces exerted on the beam.

It is worth stressing that the last integral in Eq. 1 is extended to the whole lateral surface S of the beam since $f(\mathbf{x})$ depends a priori on all the three Cartesian coordinates. A simplified, but very accurate, simulation technique consists in choosing $\mathcal{C}$ as a one-dimensional space with

$$w(y,t) = \Psi(y)x(t), \qquad \tilde{w}(y) = \Psi(y)\tilde{x},$$

where $\Psi(y)$ is the first modal shape for a doubly clamped beam:

$$\Psi(y) = B(\cos(\lambda y) - \cosh(\lambda y)) + C(\sin(\lambda y) - \sinh(\lambda y)),$$

TABLE I

DEVICES' PARAMETERS

Parameter	*Value*	
	BS	*CS*
Gap (x_0)	2.4 µm	2.0 µm
Beam length (L)	987.6 µm	
Beam width (w)	3.4 µm	
Thickness (h)	22 µm	
Young modulus (E)	150 Gpa	
Polysilicon density (ρ)	2320 kg/m^3	
Beam stiffness (k)	2.23 N/m	
Effective mass (m)	0.068 nkg	
Resonance frequency (f_0)	28.82 kHz	
Overetch spread	± 0.15 µm	
Nominal package pressure (p)	1 mbar	

with $\lambda = 4.73/L$ and

$$\frac{C}{B} = \frac{\cos(\lambda L) - \cosh(\lambda L)}{\sin(\lambda L) - \sinh(\lambda L)},$$

normalized such that $\Psi(L/2) = 1$.

Inserting the assumed interpolation in Eq. 1 one gets the standard 1D model:

$$m\ddot{x}(t) + kx(t) = F(t),$$

where

$$m = \int_0^L \rho A \Psi^2(y)\mathrm{d}y = 0.396\,\rho AL, \tag{2}$$

$$k = \int_0^L EJ(\Psi'')^2(y)\mathrm{d}y = 198.46\,EJ/L^3, \tag{3}$$

$$F(t) = \int_S f(\mathbf{x}, t)\Psi(y)\mathrm{d}S. \tag{4}$$

Two different contributions to the force F are analyzed in this paper. One is the Lorentz generalized force F_L due to the magnetic field B_x and current $i(t)$:

$$F_\mathrm{L}(t) = B_x i(t) \int_0^L \Psi(y)\mathrm{d}y = 0.523\,B_x i(t) L. \tag{5}$$

The other is the force due to the interaction of the vibrating beam with the surrounding gas, which generates the dominant dissipative contribution. This latter term is addressed in Subsection II.C.

Geometrical dimensions and extracted mechanical parameters of the presented devices are summarized in Table I. The first resonance mode of the beam, assuming the nominal width, can be calculated to be at 28.82 kHz.

B. Electrostatic Sensitivity

In this section, the electrostatic sensitivities $S_\mathrm{el} = \Delta C/\Delta x$ are predicted using Finite Element Methods (FEM), for both devices. In this context, x is assumed as the displacement of the center of the beam. The domain boundaries of the FEM simulations resemble as much as possible the fabrication process, taking into account the substrate lying beneath the structures and the oxide underneath the stators. Simulations are

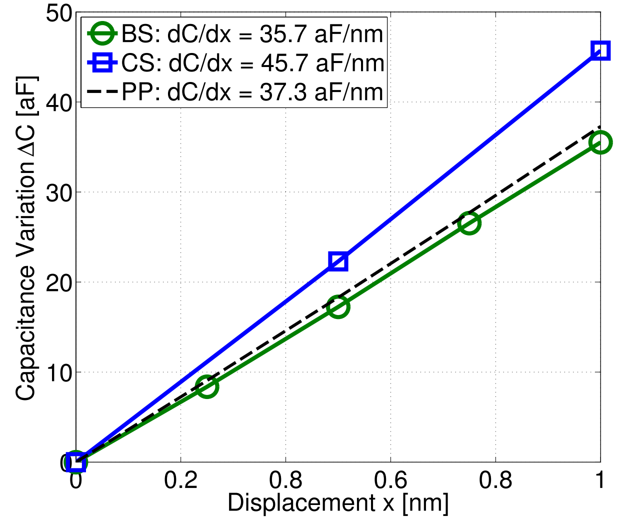

Fig. 2. Results of Comsol Multiphysics FEM simulations of the electrostatic sensitivity (i.e. the differential capacitance variation per unit displacement) of the two devices presented in this paper. The green curve (circular markers) represents the BS device, the blue curve (square markers) the CS one. For comparison, the theoretical sensitivity of a standard parallel plate device is reported (black dashed line).

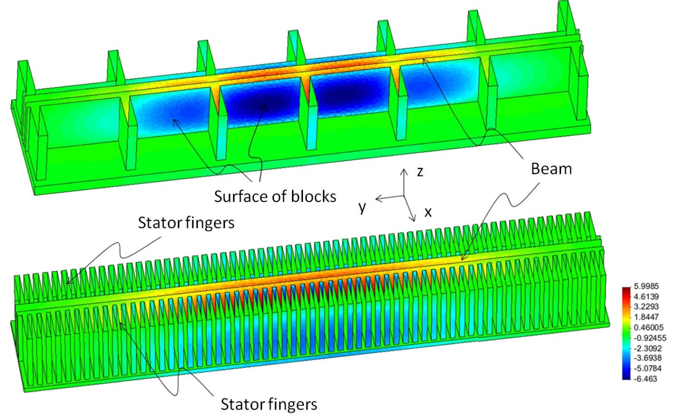

Fig. 3. Geometric models of the BS and CS devices, with the surfaces of both kinds of stators and the beam in between. The contour plot represents the non-dimensional viscous force f_b in the x direction such that, in Eq. 6, $ChL = \int_S f_\mathrm{b}(\mathbf{x})\Psi(y)\,\mathrm{d}S$, where S is the lateral surface of the beam (see also Eq. 4).

performed in three dimensions, by fixing Dirichlet boundary conditions for the substrate and the stators (grounded) and for the beam (whose voltage is set to an arbitrary DC value). Neumann conditions are set at the boundaries of the air volume surrounding the device. The FEM software solves for the electrostatics equations and gives as an output the differential capacitance variation as a function of the center displacement. Results are reported in Fig. 2. As shown, for such small values of displacement, non linear effects can be neglected. For comparison, the response of a standard parallel plate configuration with a 2.4 μm gap was also simulated.

A rough analytical estimate for the absolute value of the differential capacitance variation for a beam within two continuous stators (PP) can be obtained from:

$$S_\mathrm{el} = \frac{\Delta C}{\Delta x} = 2\varepsilon_0 \frac{h}{x_0^2} \int_0^L \Psi(y)\mathrm{d}y = 35.0\,\mathrm{aF/nm}.$$

This estimation indeed neglects all fringe effects but can be fruitfully employed for comparison with the FEM simulations.

Looking at the simulations results, one can note that the sensitivity of the block-shaped stator device ($S_{el,BS} = 35.7$ aF/nm) is slightly lower ($\approx 95\%$) than the parallel plate one, while the one of the comb-shaped stator device is even higher ($S_{el,CS} = 45.7$ aF/nm); this gain is obtained thanks to the lower gap allowed by this particular shape (see Table I). For the BS device the 5% loss in capacitance variation is due to the slight reduction of the facing area of the plates. For the CS device, the higher loss in facing area is compensated partially by the reduction of the gap and partially by increased fringing effects. The result is a capacitance variation which is 1.23 times higher than the PP one. The purpose of changing the geometry (from the standard parallel plate configuration) without worsening the electrostatic sensitivity $\Delta C/\Delta x$ is thus fulfilled.

C. Mechanical Sensitivity and Damping Modeling

Even if the MEMS of interest in the present investigation have relatively low package pressures in the range of 1 mbar, the dominant loss mechanism is still associated with the interaction of the rarefied gas with the structure.

It is worth stressing [7] that, for these devices, the Knudsen number, defined as $\mathrm{Kn} = \lambda/\ell$, where ℓ is a characteristic length of the flow (e.g. the gap between parallel plates) and λ the mean free path of gas molecules, is typically well above 10. Working conditions hence fall within the free-molecule regime where collisions between molecules can be neglected.

In [12] and [13], a deterministic integral approach has been developed to compute the gas forces in these conditions. The problem is formulated in terms of a scalar unknown representing the flux of molecules impinging on the MEMS surfaces; the viscous forces are then computed as a post-processing of the problem unknown. This technique proves to be much more efficient than the standard stochastic Test Particle Monte Carlo (TPMC) methods for the typical working conditions of gyroscopes and magnetometers, where resonant frequencies are always in the range of 2×10^4 Hz. The code developed in [13] is here applied in order to analyze the different configurations of the stators and predict the level of dissipation.

In [12] it is shown that if the following quasi static assumption holds:

$$\frac{f}{\sqrt{2\mathcal{R}T}} x_0 \ll 1,$$

where f is the vibration frequency, $\mathcal{R}$ is the universal gas constant divided by the molar mass and T is the working temperature, the contribution to the generalised force in Eq. 4 gives rise to the viscous term $F_b(t) = -b\dot{x}(t)$, with:

$$b = ChL\rho\sqrt{2\mathcal{R}T}. \tag{6}$$

In Eq. 6, ρ is the gas density, h and L are listed in Table I. The non-dimensional constant C depends only on the problem geometry and on the modal shape $\Psi(y)$ and is computed using the integral approach described earlier. For instance, and for comparison with data provided in Table II, a shuttle rigid plate vibrating in the free space at infinite distance from stator plates gives:

$$C = \frac{\sqrt{\pi}}{2} + \frac{2}{\sqrt{\pi}} \simeq 2.$$

It is clear from Eq. 6 that, at constant temperature, the viscous force is proportional, through the density, to the working pressure p.

TABLE II
EXTRACTED PARAMETERS FROM DAMPING SIMULATIONS. THE CONSTANT C IS DEFINED IN EQ. 6

Device	***C constant***	***Q-factor at 1 mbar***
PP	9.75	120
BS	7.75	150
CS	3.85	303

In Table II, C constants computed for the three different configurations described in the paper (PP, BS and CS devices) are reported. It is worth stressing that the viscous coefficient b and hence the quality factor Q can be computed for any value of pressure p. For convenience, in the last column of Table II the quality factors are listed only at the nominal working pressure of 1 mbar, for each device. Considering that the quality factor is proportional to $1/p$ in the free molecule regime, the Q value at any pressure can be easily computed starting from the third column of Table II.

Other sources of dissipation have been neglected in the 1D model. Indeed, thermoelastic losses for polysilicon beams have a lower bound on the associated quality factor of 10^4 (as discussed in [14]) which is much larger that the quality factors involved in the present investigation. Also anchor losses might in principle contribute. This topic has been addressed both theoretically and numerically in many recent works. For instance, the analytical formula proposed in [15] predicts an associated quality factor in excess of 10^9, which again suggests to neglect this source of dissipation.

III. CHARACTERIZATION MEASUREMENTS

Characterization measurements to validate the predictions of Section II were performed on both devices. In particular, quasi static capacitance-to-voltage (CV) curves and dynamic responses were evaluated, using the MEMS Characterization Platform (MCP) described in [16]–[18]. To connect the devices to the instrument, the silicon die is glued onto a ceramic carrier that is soldered to an electronic board. Through mechanical switches, the board allows both a direct connection of the MEMS electrodes to the instrument (as used in this Section) and a connection of the same electrodes to a suitable discrete-components front-end electronics for the purposes described in Section IV.

The quasi-stationary CV curves are obtained by applying a slowly increasing voltage, from 0 V up to 4.8 V to one stator; in the meanwhile, the suspended beam is kept at the ground potential and the capacitance between the beam and the second stator is measured through a high-frequency (1 MHz) signal.

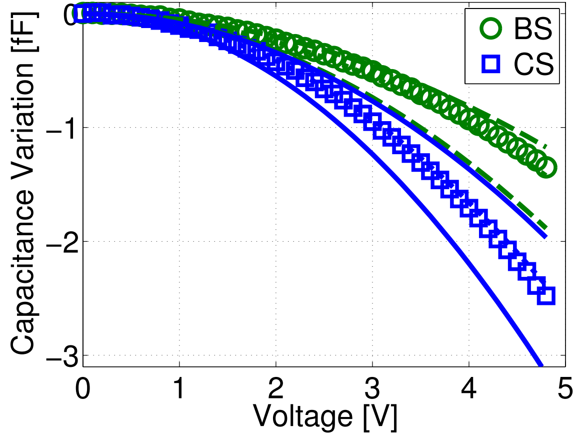

Fig. 4. Comparison between the measured CV curves and the theoretical ones (predicted both at minimum and maximum process etching). The measured points (indicated by markers) lie within the acceptable range. Circles and dashed curves refer to the BS device, squares and continuous curves to the CS one.

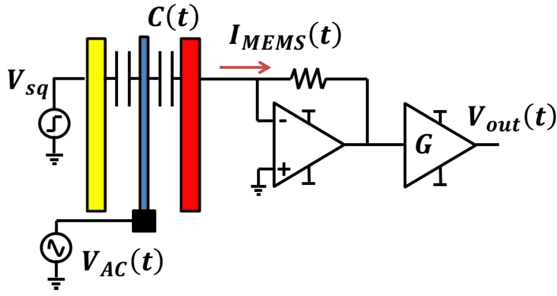

Fig. 5. Schematic of the circuit used for characterization measurements [16], [18].

Fig. 4 reports sample experimental results for both devices. For each device, the measured curves (indicated by markers) are compared with two theoretical curves (with no markers), referring to the minimum (-0.15 μm) and maximum ($+0.15$ μm) process etch spread. These curves are estimated from the spring constant predicted in Section II.A and the simulated electrostatic sensitivities of Section II.B. The results effectively lie within the process corners, suggesting a good agreement between theoretical predictions and results.

Dynamic measurements are performed to evaluate the quality factor and the resonance frequency of the structures. The used instrumentation applies voltage square waves of the desired amplitude (3 V in this work) at one stator, and measures (through the other stator capacitance) the dynamic response to the upward and downward steps of the wave. In particular, the measurement after the downward step (from 3 V to 0 V) is used, as in this situation no bias (except for the small-amplitude high-frequency readout signal) is applied to the structure, and the free oscillation can be measured. A schematic of the measurement system is shown in Fig. 5.

Examples of such measurements for both the devices are reported in Fig. 6, where the capacitance variation (on the y-axis) is plotted as a function of time (on the x-axis). The instrumentation also allows to fit the measured data with an exponentially decaying sinusoidal wave,

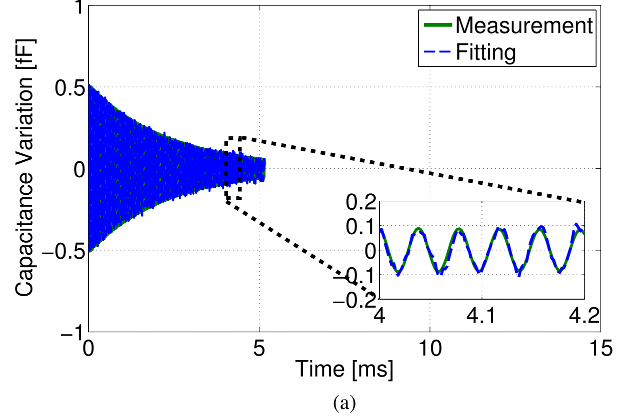

(a)

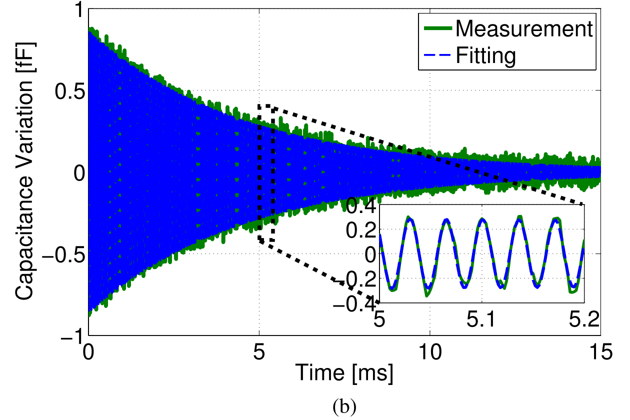

(b)

Fig. 6. Time variation of the device's capacitance after a voltage step applied to the stators. The green curve represents measured data; the blue dashed curve is the best fitting curve. Fig. 6a refers to a BS device, Fig. 6b to a CS one. The higher quality factor exhibited by the CS device in reflected in the longest time constant of the exponential decay of the amplitude of the free oscillation wave. (a) BS device. (b) CS device.

TABLE III
EXTRACTED PARAMETERS FROM CHARACTERIZATION MEASUREMENTS

Device	***Cap. var.*** [fF]	***Res. freq.*** [Hz]	***Q-factor***
BS	1.35	25354	180
CS	2.48	28214	400

that mathematically describes this step response. The obtained best fitting parameters reveal the values of the resonance frequency and quality factor.

Experimental results, extracted from characterization measurements, are summarized in Table III. CV results are in good agreement with theoretical predictions. Given the electrostatic force vs displacement relationship and the electrostatic sensitivity, one can predict the capacitance variation per unit applied volt [16]. Assuming 4.8 V applied to the stators, estimated values are 1.4 fF for BS devices and 2.5 fF for CS device, perfectly in line with the measured ones. As expected from Section II.C, both devices exhibit a higher quality factor than that estimated (see Table II) for parallel-plate (PP) sensing stators. In particular, CS devices exhibit a higher Q-factor ($\approx$400) than BS devices ($\approx$180), even if their

gap is narrower. The measured resonance frequencies are in both cases within ±10% of the predicted value.

It is worth stressing that the pressure in the closed package (nominally 1 mbar) is known to within ±10% accuracy. This anyway shows a very good predictive capability of the theoretical model.

IV. Measurements With Magnetic Field

The purpose of this Section is to combine the separate predictions about the electrostatic and mechanical sensitivities, described in Section II and validated in Section III, into an overall sensitivity under an actuating force at resonance. As a representative example in this sense, the devices were used as Lorentz-force-based capacitive MEMS magnetometers. Changing the position of the mechanical switches designed on the PCB board, the ends of the suspended beam were connected to a circuit for precise Lorentz current driving, and the MEMS stators were connected to a low-noise capacitive interface.

The differential capacitance variation (it is here assumed the two-sided difference $|\Delta C_1 - \Delta C_2|$) per unit input force, at resonance, can be written as:

$$\frac{\Delta C}{\Delta F} = \frac{\Delta C}{\Delta x} \cdot \frac{\Delta x}{\Delta F} = \frac{\Delta C}{\Delta x} \cdot \frac{Q}{k}. \tag{7}$$

Given an external magnetic field variation ΔB in the out-of-plane direction and a peak driving current i_0, the corresponding peak Lorentz force variation can be written as $\Delta F = \Delta B \cdot i_0 \cdot L$. The theoretical differential capacitance variation per unit magnetic field is thus:

$$\frac{\Delta C}{\Delta B} = \frac{\Delta C}{\Delta x} \cdot \frac{Q}{k} \cdot i_0 \cdot L. \tag{8}$$

Theoretical predictions, normalized to the driving current amplitude, are 1.15 aF/(μT mA) and 3.01 aF/(μT mA) for the BS and the CS devices, respectively. As a comparison, the same parameter, evaluated for a continuous parallel plate stators' device, turns out to be 0.97 aF/(μT mA).

Electrostatic sensitivity $\Delta C/\Delta x$ and Q-factor predictions, described in the previous Sections, are jointly verified with this kind of measurement.

A. Experimental Setup

The AC current (100 μA peak value) at the resonance frequency is injected through the beam by a suitable current driving circuit, which implements a differential Howland current scheme [19].

As described in [20], the differential capacitive readout circuit is formed by two charge amplifier stages (one per stator) with a feedback impedance formed by a resistance R_f = 600 MΩ and a capacitance C_f = 0.5 pF. AD8065 low-noise operational amplifiers by Analog Devices are used. The stators are connected to the virtual ground of the amplifiers, whose positive inputs are biased at the same constant voltage. Thanks to the feedback network, this also biases the device. The transfer function of the front-end stage is thus $\Delta V_\mathrm{out}/\Delta C_\mathrm{diff} = V_\mathrm{bias}/C_\mathrm{f}$. The output nodes of the two amplifiers are high-pass filtered and fed as inputs to an instrumentation amplifier (INA129 by Texas Instruments) whose output is thus proportional to the differential capacitance variation. A lock-in amplifier (SR830 by Stanford Research Systems) performs the demodulation, to finally obtain the information on the capacitance variation.

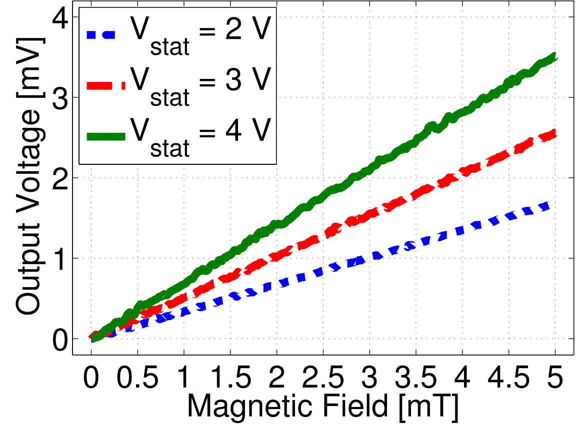

(a)

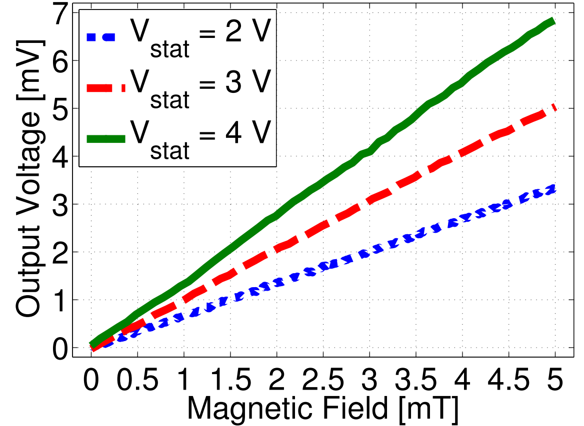

(b)

Fig. 7. Measured sensitivities at different bias voltages. 7a refers to a BS device, 7b to a CS device. (a) BS device. (b) CS device.

Note that different values of the stators' biasing voltage lead to slightly different resonance frequencies due to electrostatic softening [5]: for sake of precision, the resonance frequency of the devices was measured (with the setup described in Section III) for all the different biasing voltages used in the next subsection, in order to precisely guarantee resonant operation of the devices.

The magnetic field is generated by a triaxial Helmholtz coils system, from Micromagnetics Inc.; the instrument range is ±6 mT, with a maximum frequency of time-varying (sinusoidal) fields of about 200 Hz.

The overall sensitivities were calculated applying an increasing magnetic field along one axis of the Helmholtz coils system, from 0 to +5 mT, and measuring the output signal. Bandwidth measurements were performed applying an AC input magnetic field with an amplitude of 4 mT at different frequencies, in the range 1 Hz-100 Hz, and measuring the corresponding output signal.

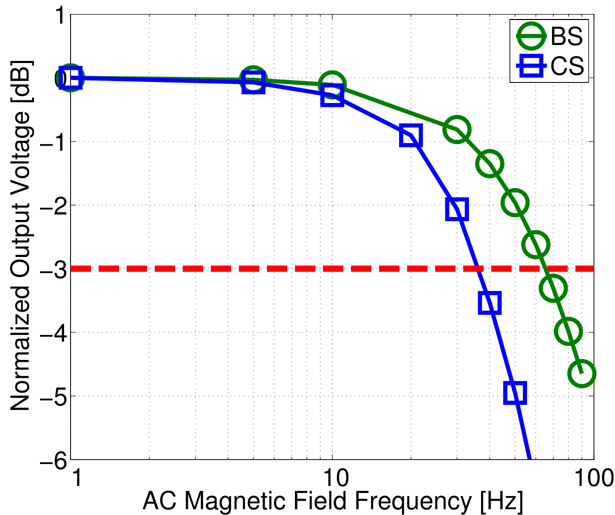

Fig. 8. Normalized output voltages as a function of the AC input magnetic field frequency. Measurements are shown for one sample of both devices, BS (green, circles) and CS (blue, squares).

B. Results

In Fig. 7, the differential voltage at the front-end output is shown as a function of the input DC magnetic field, for different bias values of the sensing stators. From shown measured data and using the transfer function of the front-end stage, one can then extrapolate the device sensitivity to magnetic fields $\Delta C/\Delta B$, which is independent from readout electronics and bias voltage.

The differential capacitance variation per unit magnetic field, normalized to the AC Lorentz driving current $\Delta C/(\Delta B \cdot i_0)$, can be extracted, for comparative purposes with other works. The obtained values are 1.5 aF/(μT mA) for the BS device and 3.5 aF/(μT mA) for the CS device, reasonably in line with the predictions.

These results can be compared to the one obtained for a typical multi-parallel-plate configuration built with the same fabrication process [6], whose value at resonance is 0.8 aF/(μT mA). One can conclude that the presented structures provide a significant performance improvement.

As a further verification of the quality factors, AC measurements were performed with time-varying sinusoidal magnetic fields, applied at different frequencies. The corresponding output signal was measured, and the amplitudes (normalized to the maximum value) are reported in Fig. 8, as a function of the AC input magnetic field frequency. One can then extract the bandwidth of the system, by evaluating the frequency where the output signal amplitude is -3 dB (i.e. $1/\sqrt{2}$) lower than the maximum. Bandwidths of $\Delta f_{\mathrm{BS}} = 64$ Hz and $\Delta f_{\mathrm{CS}} = 34$ Hz are found, in line to what predicted by the relationship $\Delta f = f_0/(2Q)$, for both devices. As expected, the maximum sensing bandwidth reduces with increasing quality factors.

V. Conclusion

The work demonstrated how the performances of resonant capacitive inertial MEMS can be improved with a change of the sensing stators geometry, in particular with the introduction of suitable ways-out for gas molecules, that determines a reduction of the damping coefficient with almost no impact on the value of the capacitance and of its variation with displacements. This leads to an increase of the quality factor of the system, thus improving sensitivity and resolution in resonant operation.

Theoretical predictions about this behavior were experimentally verified on suitable resonant beams, both through electro-mechanical characterization measurements (static and dynamic) and by operating the devices as Lorentz-force magnetometers.

We are planning to investigate in the near future the effect of these ways-out with a wider variety of sensing stator geometries, in order to find the optimum layout that guarantees the best performances.

The same principle presented in this work can be as well applied to boost the quality factor without changing the package pressure in other devices, like resonant accelerometers [21], or MEMS oscillators in the range 10 kHz-100 kHz [22].

The solution could be effective also with mode-split operated devices [23] where very low damping coefficients are desired to lower the MEMS thermo-mechanical noise.

References

[1] B. Vigna, "Tri-axial MEMS gyroscopes and six degree-of-freedom motion sensors," in *Proc. IEEE Int. Electron Devices Meeting (IEDM)*, Dec. 2011, pp. 29.1.1–29.1.3.

[2] N. Yazdi, F. Ayazi, and K. Najafi, "Micromachined inertial sensors," *Proc. IEEE*, vol. 86, no. 8, pp. 1640–1659, Aug. 1998.

[3] W. A. Clark, "Micromachined Z-axis vibratory rate gyroscope," U.S. Patent 5 992 233, Nov. 30, 1999. [Online]. Available: http://www.google.com/patents/US5992233

[4] H. Emmerich, M. Schofthaler, and U. Knauss, "A novel micromachined magnetic-field sensor," in *Proc. 12th IEEE Int. Conf. Micro Electro Mech. Syst. (MEMS)*, Jan. 1999, pp. 94–99.

[5] V. Kempe, *Inertial MEMS*. Cambridge, U.K.: Cambridge Univ. Press, 2011.

[6] G. Langfelder, C. Buffa, A. Frangi, A. Tocchio, E. Lasalandra, and A. Longoni, "Z-axis magnetometers for MEMS inertial measurement units using an industrial process," *IEEE Trans. Ind. Electron.*, vol. 60, no. 9, pp. 3983–3990, Sep. 2013.

[7] A. Frangi, A. Frezzotti, and S. Lorenzani, "On the application of the BGK kinetic model to the analysis of gas-structure interactions in MEMS," *Comput. Struct.*, vol. 85, nos. 11–14, pp. 810–817, Jun. 2007.

[8] K. Persson and K. Boustedt, "Fundamental requirements on MEMS packaging and reliability," in *Proc. 8th Int. Symp. Adv. Packag. Mater.*, 2002, pp. 1–7.

[9] A. Frangi, B. De Masi, G. Langfelder, and D. Paci, "Optimization of Lorentz-force MEMS magnetometers using rarefied-gas-theory," in *Proc. IEEE SENSORS*, Nov. 2013, pp. 1–4.

[10] G. Langfelder, S. Dellea, F. Zaraga, D. Cucchi, and M. A. Urquia, "The dependence of fatigue in microelectromechanical systems on the environment and the industrial packaging," *IEEE Trans. Ind. Electron.*, vol. 59, no. 12, pp. 4938–4948, Dec. 2012.

[11] F. D. Bannon, J. R. Clark, and C. T.-C. Nguyen, "High-Q HF microelectromechanical filters," *IEEE J. Solid-State Circuits*, vol. 35, no. 4, pp. 512–526, Apr. 2000.

[12] A. Frangi, "A BEM technique for free-molecule flows in high frequency MEMS resonators," *Eng. Anal. Boundary Elements*, vol. 33, no. 4, pp. 493–498, 2009.

[13] A. Frangi, A. Ghisi, and L. Coronato, "On a deterministic approach for the evaluation of gas damping in inertial MEMS in the free-molecule regime," *Sens. Actuators A, Phys.*, vol. 149, no. 1, pp. 21–28, 2009.

[14] R. Ardito, C. Comi, A. Corigliano, and A. Frangi, "Solid damping in micro electro mechanical systems," *Meccanica*, vol. 43, no. 4, pp. 419–428, 2008.

[15] I. Wilson-Rae, "Intrinsic dissipation in nanomechanical resonators due to phonon tunneling," *Phys. Rev. B*, vol. 77, p. 245418, Jun. 2008.

[16] G. Langfelder, A. Longoni, and F. Zaraga, "Low-noise real-time measurement of the position of movable structures in MEMS," *Sens. Actuators A, Phys.*, vol. 148, no. 2, pp. 401–406, Dec. 2008.

[17] C. Buffa, A. Tocchio, and G. Langfelder, "A versatile instrument for the characterization of capacitive micro- and nanoelectromechanical systems," *IEEE Trans. Instrum. Meas.*, vol. 61, no. 7, pp. 2012–2021, Jul. 2012.

[18] *MEMS Characterization Platform, MCP-A-04, Product Data-Sheet*, ITMEMS s.r.l., Milano, Italy, May 2014. [Online]. Available: http://www.itmems.it

[19] D. H. Sheingold, "Impedance & admittance transformations using operational amplifiers," *Lightning Empiricist*, vol. 12, no. 1, pp. 1–8, 1964.

[20] G. Langfelder, G. Laghi, P. Minotti, A. Tocchio, and A. Longoni, "Off-resonance low-pressure operation of Lorentz force MEMS magnetometers," *IEEE Trans. Ind. Electron.*, vol. 61, no. 12, pp. 7124–7130, Dec. 2014.

[21] T. A. Roessig, R. T. Howe, A. P. Pisano, and J. H. Smith, "Surface-micromachined resonant accelerometer," in *Proc. Int. Conf. Solid-State Sens. Actuators (TRANSDUCERS) Chicago*, vol. 2. Chicago, IL, USA, Jun. 1997, pp. 859–862.

[22] W. C. Tang, T.-C. H. Nguyen, and R. T. Howe, "Laterally driven polysilicon resonant microstructures," in *Proc. Invest. Micro Struct., Sens., Actuators, Mach., Robots, IEEE Micro Electro Mech. Syst.*, Feb. 1989, pp. 53–59.

[23] G. Langfelder and A. Tocchio, "Operation of Lorentz-force MEMS magnetometers with a frequency offset between driving current and mechanical resonance," *IEEE Trans. Magn.*, vol. 50, no. 1, pp. 1–6, Jan. 2014, Art. ID 4700106.